Impact of inflow conditions and turbine placement on the performance of offshore wind turbines exceeding 7 MW

Konstantinos Vratsinis[1,2], Rebeca Marini[1,2], Pieter-jan Daems[1,2], Lukas Pauscher[1,4,5], Jeroen van Beeck[3,1], and Jan Helsen[1,2,6]

[1]Acoustics and Vibrations Research Group (AVRG), Vrije Universiteit Brussel, Pleinlaan 2, Ixelles, Brussels, 1050, Belgium
[2]OWI-Lab, Pleinlaan 2, Brussels, 1050, Belgium
[3]The von Karman Institute for Fluid Dynamics, Waterloosesteenweg 72, Sint-Genesius-Rode, 1640, Belgium
[4]Department of Sustainable Electrical Energy Systems, University of Kassel, Wilhelmshöher Allee 71-73, Kassel, 34121, Germany
[5]Fraunhofer Institute for Energy Economics and Energy System Technology (IEE), 34117 Kassel, Germany
[6]Flanders Make @ VUB, Pleinlaan 2, 1050 Brussels, Belgium

Correspondence: Konstantinos Vratsinis (konstantinos.vratsinis@vub.be)

Abstract.

Accurately assessing wind turbine performance in large offshore wind farms requires a nuanced understanding of how inflow parameters~~—~~, turbulence intensity (TI), wind shear, and wind veer~~—~~, affect power production across different turbine rows. In this study, we analyze 13 months of ~~10 – minute~~ 10 min operational data from more than 40 high-capacity turbines in a North Sea offshore wind farm, complemented by nacelle-based ~~LiDAR~~ lidar measurements of inflow. Our objectives are to (1) determine how power production differs between front, middle and rear sections of the farm under the influence of TI, shear, and veer, and (2) evaluate the effectiveness of International Electrotechnical Commission (IEC)–based normalization methods, including Rotor Equivalent Wind Speed (REWS) and turbulence corrections in the front row and inside a wind farm consisting of large-scale wind turbines.

The results indicate that the impact of wind shear and veer on power output is strongly dependent on the turbine location: ~~free stream~~ free-stream shear and veer correlate negatively with active power in the front row, yet show positive correlations in the mid and rear rows. In addition, the TI in the wake region has a distinct influence on power production~~—~~, particularly at lower wind speeds~~—~~, relative to the TI observed in the ~~free-flow~~ free-stream region. Finally, the rear section of the wind farm exhibits approximately ~~20%~~ 30% lower variability in active power relative to the front section. These location-specific changes underscore the evolving nature of inflow conditions within large wind farms. Furthermore, IEC-based REWS do not fully capture the effects of shear and veer in a large scale wind ~~turbine~~ turbines in an offshore environment. The findings highlight that turbines operating in ~~non-free-flow~~ non-free-stream conditions may require additional inflow-characterization parameters beyond standard IEC norms to achieve more accurate performance evaluations and enhance overall farm efficiency. To our knowledge, this is among the first empirical assessments spanning the front, mid, and rear sections of a modern offshore wind farm to evaluate IEC-based REWS and TI normalizations, revealing location- and regime-dependent limits and motivating complementary inflow descriptors for wake-affected operation.

~~Offshore Wind Farm Power Performance Inflow Conditions Turbine Placement Wake Effects IEC Normalization Turbulence Intensity (TI) Wind Shear and Veer Rotor Equivalent Wind Speed (REWS)~~

1 Introduction

Global wind energy capacity continues to grow at an unprecedented rate, with new installations reaching ~~123 GW~~ 123 GW (World Wind Energy Association, 2024) worldwide in 2024, largely driven by robust climate policy commitments such as the EU REPowerEU Plan (Commission, 2022) and the US Inflation Reduction Act (Congress, 2022). Although this expansion brings the international community closer to meeting ambitious decarbonization targets, it also underscores a host of technical and economic challenges. Among these are the high costs of operations and maintenance (O&M), particularly in offshore projects, and the need to optimize the power production of turbines that are increasing in size (Ren et al., 2021).

Today, onshore wind turbines frequently exceed ~~4 MW~~ 4 MW in capacity, while offshore machines of ~~8 MW~~ 8 MW or more are becoming increasingly common ~~(of Energy, 2024; McCoy et al., 2024; Rohrig et al., 2019; Vratsinis et al., 2024; Kelly and van der La~~ (of Energy, 2024; McCoy et al., 2024; Rohrig et al., 2019; Kelly and van der Laan, 2023). Factors such as turbulence intensity (TI), air density, wind shear, wind veer, and atmospheric stability significantly influence both their power output and structural loading (Dimitrov et al., 2015; Martin et al., 2020; Sumner and Masson, 2006). Although larger turbines offer higher rated capacities and energy yields, their sensitivity to variations in inflow conditions can differ compared to smaller ones. For example, (Chamorro et al., 2015) demonstrated that only turbulent structures exceeding the rotor diameter can substantially affect power output, while (Van Sark et al., 2019) showed that only wind turbines with a large rotor diameter to hub-height ratio can be significantly influenced by wind shear.

Although inflow effects have been studied numerically for both ~~free-flow~~ free-stream and wake conditions (Saint-Drenan et al., 2020; Sebastiani et al., 2023, 2024), most studies based on operational data have mainly focused on small to medium-sized turbines (~~1.5–4 MW~~ 1.5 − 4 MW) operating in relatively undisturbed wind conditions (Gottschall and Peinke, 2008; Wagner et al., 2009; Murphy et al., 2020; Clifton and Wagner, 2014; Bardal and Sætran, 2017; Kim et al., 2021; Mata et al., 2024; Gao et al., 2021; Wagner et al., 2011). Many studies explore the effect of wake on power production from the perspective of velocity deficit (Adaramola and Krogstad, 2011; González-Longatt et al., 2012), but relatively few investigate the power performance of wind turbines within wind farms under waked conditions. Consequently, while turbines inside wind farms often experience inflow conditions that deviate significantly from free-stream~~flow~~, the impact of these deviations on power production remains relatively unexplored. Most prior studies treat wake effects primarily as mean-flow (velocity) deficits and evaluate power fluctuations with respect to a free-stream reference. For example, (Seifert et al., 2021) shows that the standard deviation of the power increases with row index. In this study we condition on the local SCADA hub-height wind speed and quantify within-bin variability using identical IEC-style wind-speed bins, enabling comparisons between regions of the wind farm that are not driven by differences in mean wind speed.

Industry-standard normalization procedures for evaluating wind turbine performance are outlined by the International Electrotechnical Commission (IEC) (IEC, 2022). These methods correct for environmental factors such as TI, air density, wind shear, and veer, and are widely used to compare the performance of different turbines under various conditions. However, they were developed primarily with single, isolated turbines in mind, and their applicability to the wake-affected regions of large wind farms is not recommended and has not yet been explored. Indeed, recent work suggests that standard IEC-based turbulence corrections can both overcompensate and undercompensate for inflow TI, potentially leading to inaccuracies in power curve ~~estimations~~ estimates (Lee et al., 2020).

~~Motivated by the growing size of offshore wind projects and the scarcity of studies based on large-scale offshore wind turbines~~To address these gaps, this study ~~uses extensive real-world operational data from a large offshore wind farm to address two main questions. First, we investigate how inflow parametersand specifically TI, wind~~ aims to answer three questions: (Q1) How do inflow parameters, TI, shear, and veer~~impact —~~—affect power production across ~~different segments of an~~ the front, mid, and rear sections of a modern offshore wind farm ~~that includes wind turbines exceeding 7 MW rated power . Second, we answer to~~ with turbines exceeding 7 MW? (Q2) How does *short-term* power variability differ across these sections? (Q3) To what extent do ~~the established IEC-based normalization and correction methods~~ IEC normalization methods (REWS and the TI correction) mitigate these inflow ~~effects in~~ dependencies in both free-stream and ~~highly~~ wake-affected ~~segments of the wind farm . By examining real-world SCADA data and applying industry-standard corrections, the study aims to clarify whether current IEC methods remain robust for modern wind turbines or require further refinement,~~ conditions?

We test three hypotheses: (H1) the coupling between inflow descriptors (TI, shear, veer) and power production is *location dependent* within the farm (front vs. mid vs. rear); (H2) IEC-style normalizations (REWS for shear/veer and the TI correction) *reduce* apparent coupling near free-stream conditions but are *insufficient or regime dependent* in wake-affected rows; and (H3) wake-induced TI differs in effect from free-stream TI, especially below rated, leading to distinct correlation patterns and sensitivities across sections. Using 13 months of SCADA and upstream lidar wind speed profiles, we evaluate how the IEC normalization procedures behave in free-stream and ~~it also explores the possibility of applying these methods across an entire wind farm. Ultimately, these insights are intended to improve the accuracy of large~~ wake-affected sections of a modern offshore wind farm~~performance assessments and help reduce uncertainties in both technical design and financial planning~~.

This study provides three contributions: (i) a section-by-section (front/mid/rear) empirical analysis of how TI, shear, and veer correlate with power; (ii) a direct, within-farm evaluation of IEC normalizations (REWS, TI) that quantifies pre/post-correction changes; and (iii) evidence that downstream rows exhibit lower power variability, measured via the median absolute deviation (MAD), and different TI coupling, motivating the need of inflow descriptors beyond current IEC parameters for wake-affected wind turbines.

The paper is organized as follows. Section 2 describes the datasets and filtering methods. Section 3 outlines the methodology, including the selection of specific sections of the wind farm, the corrections implemented, the correlation analyses conducted, and the variability analysis. Section 4 presents our results, examining each of the three corrections individually. Finally, Section 5 summarizes and discusses the key findings.

2 Data collection and filtering

The study uses 13 months of data from an offshore wind farm located within the Belgian maritime area. This wind farm comprises over 40 turbines positioned more than 30 kilometers from the coastline. The prevailing wind direction is from the southwest, which predominantly influences the performance of the wind farm.

For the analysis, two different datasets are used:

SCADA data: Collected from the wind turbines, providing real-time operational information. This includes wind speed, active power, turbulence intensity (TI), and direction measured by the SCADA system using a combination of cup anemometers, wind vanes, and sonic anemometers mounted on each turbine's nacelle.

LiDAR data: ~~Measured~~ A nacelle-mounted, continuous-wave (CW) ZX TM nacelle lidar (ZX Lidars) installed at a nearby wind farm ~~approximately $8km$ away (see figure 1) . A continuous-wave nacelle-based LiDAR (ZX TM) is used to estimate wind shear and veer. The LiDAR data are averaged over $30-min$ periods for calculating wind shear and veer. Given the position of the LiDAR relative to the selected wind sector, we assume that the estimated shear and veer are representative of the entire wind farm. Therefore, the travel time to reach different sections of the wind farm has not been considered during this analysis.~~ at a distance 23.5 km (see Fig. 1) delivers two line-of-sight (LOS) speeds at six heights per profile. LOS focus is set at approximately 2 rotor diameters upstream ($\approx 420\,\mathrm{m}$) to limit local induction effects from the host turbine. Lidar profiles are smoothed with a centered 30 min rolling window and evaluated at a 10 min cadence to match SCADA. To account for the large lidar–farm separation, the lidar time series are shifted by an advection delay

$$\tau_{jk} = \frac{s_{jk}}{U_{jk}^{\mathrm{adv}}},$$

where s_{jk} is the streamwise separation from the lidar focus to turbine k at time window j, and U_j^{adv} is the centered 30 min rolling mean of the lidar measured wind speed over the same window.

2.1 Data filtering

Several filtering steps are applied to the combined dataset to ensure data validity:

1. **Data availability**: Data from ~~$1-sec$~~ 1 s measurements are aggregated into ~~$10-min$~~ 10 min averages, allowing up to 100 seconds of missing data per ~~$10-min$~~ 10 min window. This tolerance increased data availability without significantly impacting the uncertainty of the aggregated values.

2. **Turbine operational regime and environmental dynamics**: ~~Only data from operational turbines , as indicated by SCADA operational status codes, are included.~~ To ensure consistent operating conditions and wake interactions across the wind farm, a 10 min interval is kept only when all turbines are operating simultaneously. Data periods during which any of the studied turbines reported a fault or were curtailed for extended periods due to maintenance were excluded

from the dataset. However, short-term operational curtailments, which are part of the normal control strategy of a large wind farm, were not filtered out. These events occur primarily at wind speeds above the rated power, a region of less focus for this study, and their inclusion ensures that the analysis remains representative of realistic farm-wide operating conditions. Beyond these operational filters, we intentionally retain dynamic atmospheric periods by foregoing an explicit stationarity filter (i.e., no ramp/gust screening). This ensures the dataset reflects the operating conditions actually experienced by the farm and guards against overstating relationships based on selectively filtered periods.

3. **Data sanity**:

   Low variability:~~$10-min$~~ $10\,\mathrm{min}$ intervals where the standard deviation of wind speed or active power was less than 0.01% of its mean value are removed to eliminate erroneous data points marked as rejected data.

   Outliers (HDBSCAN): ~~Outliers with respect to the power curve were identified and excluded from the dataset using the DBSCAN (~~Operating states inconsistent with the nominal power curve are removed using HDBSCAN (Hierarchical Density-Based Spatial Clustering of Applications with Noise)~~algorithm, utilizing~~ (McInnes et al., 2017) in a two-dimensional space defined by rotor wind speed and ~~active power as~~ the ~~two feature dimensions for clustering.~~ active-power residual relative to the manufacturer power curve. Clustering uses a Euclidean metric, a minimum cluster size of 200, a minimum samples setting of 1, the excess-of-mass selection with $\varepsilon = 5$, and excludes trivial single-cluster solutions. Points classified as noise are excluded, and valid operating states are taken as the largest cluster. HDBSCAN excludes operating states far from the nominal curve, which can shrink the power-deviation (PD) spread and dampen correlations. To limit this, our inference relies on row-to-row contrasts and pre/post corrections changes rather than absolute variance.

4. **~~Wind sector~~ Wind-sector selection**: The analysis focused on the ~~wind sectorranging from 180° to 285°~~ $180°$–$285°$ sector, which accounted for approximately ~~50% of the observations (see~~ 64% of observations during the study period (Fig. 2)~~during the study period. This specific sector was chosen to ensure that the LiDAR~~. This sector captures the dominant energy inflow while ensuring that the lidar is measured upwind of the wind farm and is ~~free from wake effects. This selection allows for accurate estimation of wind~~ not affected by far wake contamination, enabling accurate estimation of wind shear and veer. Choosing a broader sector preserves sufficient counts per wind-speed bin for robust statistics and mitigates sensitivity to persistent narrow-azimuth wake effects (e.g., half wake condition). Turbines are grouped into front, mid, and rear sections, and for each section observations are averaged across this sector. Thereby focusing on each section's mean response to sector-averaged inflow (including wake effects).

5. **Lidar–farm representativeness.**

   The large separation between the nacelle lidar and the wind farm is a practical limitation that introduces sampling mismatch and likely attenuates the observed inflow–power correlations relative to what would be obtained with a reference directly upwind of the farm. We therefore treat the nacelle-lidar inflow variables as an upstream proxy and report two indications that this proxy is reasonable.

We assess consistency between front-row SCADA hub-height wind speed and the advection-corrected lidar reconstruction. For each 10 min record j and front-row turbine k, we pair $U_{hub}^{\mathrm{SCADA}}(t_j)$ with $U_{hub}^{\mathrm{lidar}}(t_j - \tau_{jk})$. After correcting for advection, the lidar reconstruction tracks the front-row SCADA hub-height wind speed closely. Across paired $10\,\mathrm{min}$ records, the two series have a Pearson correlation of $r = 0.88$, a near-zero mean bias of $-0.06\ \mathrm{m\,s^{-1}}$, and a root-mean-square error of $1.99\ \mathrm{m\,s^{-1}}$. These values indicate strong co-variability with only small average offset.

To evaluate spatial homogeneity of the inflow across the lidar–farm separation, we use the regional NORA3 reanalysis. NORA3 has been developed and validated for offshore wind applications and provides hourly wind speed and vertical profiles from which shear and veer ~~.~~ can be derived, suitable for assessing inflow variability Solbrekke et al. (2021) . Comparisons with profiling Doppler lidars indicate that NORA3 matches ERA5 offshore and often outperforms it in coastal settings, with agreement improving with height Cheynet et al. (2025). Using NORA3, we compare hourly shear and veer at the grid point nearest the lidar with the grid point nearest the upwind front row via Q-Q plots and coincident-hour time series (App. B). Agreement is strong across common conditions, with differences limited to extreme shear/veer. This pattern is expected, since extreme shear and veer are often spatially localized and intermittent; excluding such extremes focuses the comparison on the inflow that governs most operating periods.

Consequently, we retain only intervals for which the lidar-estimated shear α and veer β fall within the central 95% of their empirical distributions (2.5th–97.5th percentiles), specifically $\alpha \in [-0.05, 0.21]$ and $\beta \in [-3, 21]°/100\,\mathrm{m}$. These criteria, together with the advection correction, support the representativeness of the advected lidar-derived α and β as upstream inflow descriptors.

After these filtering steps, the final dataset comprised over ~~$600{,}000\ 10 - min$~~ $600.000\ 10\,\mathrm{min}$ intervals, representing approximately 25% of the raw data for the studied wind sector. The resulting accepted and rejected sets are shown in Fig. 3.

3 Methodology

This study evaluates the correlation of environmental parameters across different sections of a wind farm. It also assesses the potential application of IEC corrections in SCADA-based performance evaluations within an offshore wind farm, specifically by examining their impact on correlations with power production and the variance of the power curve. To achieve the objectives of the study, after the collection and filtering of the data, the following procedure is followed:

Section division: The dataset is divided into three sections: the front (first row with free-stream inflow), the mid (middle section), and the rear (end of the farm).

Active power normalization: Power production is normalized using the power curve of the manufacturer.

IEC corrections: The wind speed and the power output are adjusted using the IEC corrections IEC (2022) for wind shear-veer and TI.

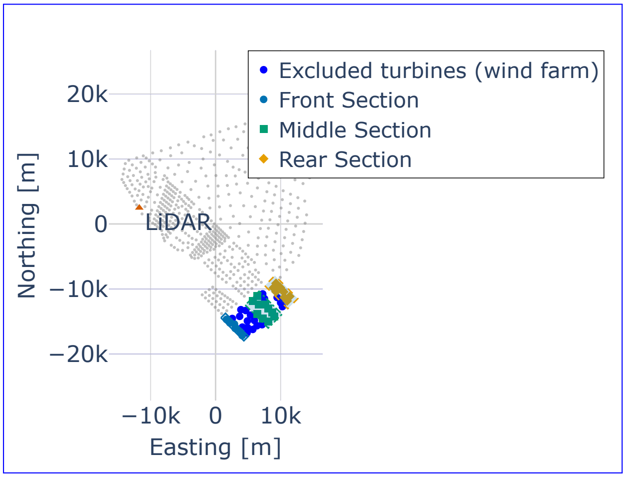

Figure 1. Wind farm layout showing the ~~LiDAR~~ lidar system and the designated study sections for southwest wind conditions. ~~Gray~~ Black dots represent the wind turbines within the wind farm that were excluded from the study and light gray dots are other wind farms within the same cluster given for context.

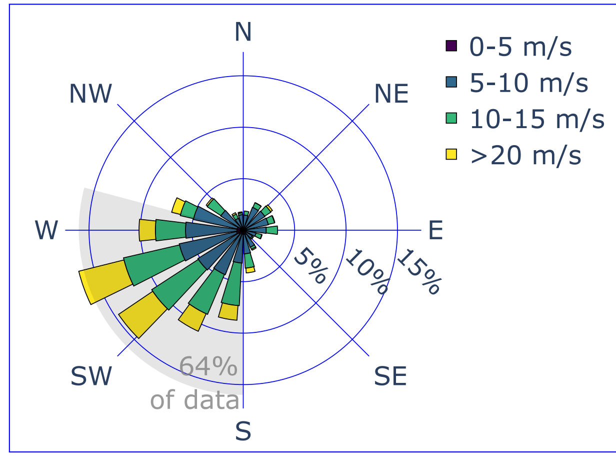

Figure 2. Wind rose illustrating the distribution of wind directions and rotor wind speeds, highlighting the study region where ~~50%~~ 64% of the data points are concentrated.

Correlation analysis: Correlation analysis is performed between environmental parameters and active power before and after the IEC corrections for each section. The effect of IEC corrections is then evaluated.

Variance analysis: The variance of the active power is traced over different wind speeds, both before and after the IEC corrections, for each section. The effect of IEC corrections on the power variability is then evaluated.

These steps are further explained in the following sections of this paper.

3.1 Section division

Free-flow wind turbines are defined in accordance with the IEC 61400-12-1:2022 IEC (2022) standard, which specifies the criteria for an undisturbed region by accounting for the influence of adjacent wind turbines and obstacles. We apply the recommended method to calculate the valid sectors for each wind turbine in the wind farm, selecting those in the first row that met the standards as ~~free-flow turbines.~~ free-stream turbines. Throughout, we consider these front-row free-stream turbines to represent the site's free-stream TI. The middle and rear sections are defined based on the distance to the nearest free-stream wind turbine measured along the flow direction. The sections widths are defined so as to ensure they contain a volume of data comparable to that from ~~free-flow wind turbines—approximately $160,000$ $10-min$~~ free-stream wind turbines, approximately $156,000$ $10\,\mathrm{min}$ intervals per section. Hence, the datasets are balanced and easily comparable. Figure 1 illustrates the segmentation of the wind farm into these three sections. The wind turbines shown in black in Fig. 1 are intentionally omitted to increase the spacing between sections and produce clearer and more interpretable trends.

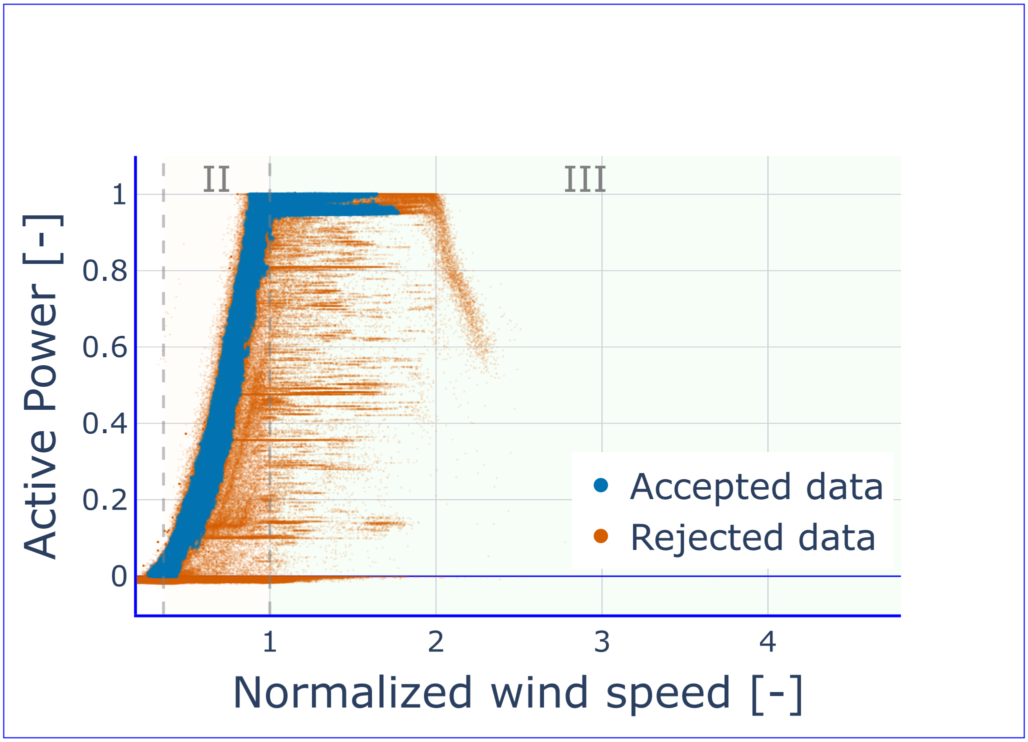

Figure 3. The raw dataset is shown: ~~green~~ blue indicates the accepted data used in this study, and ~~red~~ orange denotes the rejected data. The region II is referring to torque control region and region III to pitch control

3.2 Active power deviation

This study examines how each environmental parameter positively or negatively contributes to power output at various locations within a wind farm and across different wind speeds. To isolate the influence of these environmental variables while minimizing the effect of variations in wind speed within each bin, we employ the concept of power deviation (PD) to normalize the active power, as described below:

$$PD_i = P_{\text{measured},i} - P_{\text{manufacturer},i} \tag{1}$$

where $P_{\text{measured},i}$ refers to the measured power at the i^{th} wind speed bin, and $P_{\text{manufacturer},i}$ refers to the power given by the power curve of the manufacturer at the i^{th} wind speed bin.

3.3 Inflow metrics from nacelle lidar

Upstream inflow shear (α) and veer (β) are derived from the nacelle lidar wind speeds described in Sec. 2. Each lidar wind speed profile is based on two LOS at six heights, at a range $\sim$2 rotor diameters upstream. Assuming negligible vertical velocity and mean yaw alignment, horizontal speed $U(z)$ and direction $\theta(z)$ at the sampled heights are reconstructed from the symmetric LOS pair and regressed against $\ln(z/z_{\text{ref}})$; the slopes give α (dimensionless) and β (reported in $°/100\,\text{m}$). The expanded instrumental uncertainties for $30\,\text{min}$ means are small relative to the natural variability ($U_\alpha \approx 0.01$ at $\alpha = 0.3$ and $U_\beta \approx 0.15°/100\,\text{m}$; $k = 2$) see App. A for details. We treat these upwind α and β as boundary conditions for the front section, not as invariants within the array; their wake-modified evolution across rows is analyzed by our front/mid/rear methodology.

3.4 IEC corrections

The atmospheric boundary layer in which a wind turbine operates is a dynamic environment. Different inflow conditions are expected to produce varying power outputs at a wind speed. However, collecting sufficient data in a short time frame for every possible inflow condition to create a multi-variable power curve is practically impossible. The IEC standards recommend a combination of corrections to wind speed and active power to reduce the dependency of power output on environmental parameters. One of the goals of this study is to assess the correlation between each environmental parameter and power output across different sections of the wind farm and evaluate the effectiveness of existing IEC corrections in these sections. Ideally, after applying the corrections, the correlation between the environmental parameters and power output should approach zero. This section will briefly discuss the corrections applied in this study.

3.4.1 Wind shear and veer correction

For wind turbines with large rotor diameters, variability in wind speed and direction across the rotor can significantly affect power production. This study employs ~~LiDAR~~ lidar measurements taken upstream near the wind farm to evaluate the shear and veer coefficients of the wind. The derived coefficients enable estimation of wind speed and direction at different heights based on the average shear and veer profiles.

According to IEC standards (IEC, 2022), the REWS is defined as:

$$v_{\text{rews}} = \left(\sum_{i=1}^{n} \left(v_i \cos(\phi_i) \right)^3 \frac{A_i}{A} \right)^{1/3}, \tag{2}$$

where n is the number of available measurement heights; v_i is the wind speed calculated at height i based on the shear exponent and the hub height wind speed; ϕ_i is the calculated angle difference between the rotor direction and the wind speed at height i based on the measured difference at hub height; A is the swept rotor area; A_i is the i^{th} segment area.

To assess the individual contributions of shear and veer to the REWS, we compute the REWS under two separate conditions: one that excludes veer ($\phi = 0$) and one that excludes shear ($u_i = u_{hub\,height}$). The resulting REWS values are then applied to normalize the wind speed according to the IEC standard.

3.4.2 Turbulence Intensity (TI) correction

TI can significantly impact the power output of a wind turbine, particularly within a wind farm, where TI tends to increase (Barthelmie et al., 2007), potentially biasing the power curves across different sections. Because wakes increase TI, absolute

$|\rho|$ can be inflated; therefore, we emphasize between-section differences and $\Delta|\rho|$ rather than solely absolute magnitudes. This study employs the TI normalization recommended by the IEC to model the effects of ~~$10-min$~~ 10 min averaging on power output.

A complete discussion of the normalization process is outside the scope of this paper and is well documented in the IEC standard (IEC, 2022); here, we provide an overview for completeness. The first step is to calculate the zero turbulence power curve. The zero turbulence power curve represents the theoretical power output of a wind turbine under idealized conditions in which the wind is completely steady. The normalization process adjusts the active power measured during a ~~10-minute~~ 10 min interval by first subtracting a simulated average power~~—~~, calculated using the ideal zero TI power curve and the measured wind distribution~~—~~, and then adding a simulated average power~~—~~, calculated using the ideal zero TI power curve and a Gaussian wind speed distribution corresponding to the reference TI. ~~The~~ Simulated average power in the contex of the IEC standard is the expectation of the zero-turbulence curve P_0 under a wind-speed distribution centered at the 10 min mean wind speed v_j (where j indexes 10 min records). Following the IEC, wind speed is modeled as Gaussian with mean $\mu = v_j$ and standard deviation $\sigma = I\,v_j$ for the measured TI I (of record j), and $\sigma = I_{\mathrm{ref}}\,v_j$ for the reference TI I_{ref}. With this definition, the normalization is given by:

$$\overline{P}_{I_{\mathrm{ref}}}(v) = \overline{P}(v) - \overline{P}_{\mathrm{sim},I}(v) + \overline{P}_{\mathrm{sim},I_{\mathrm{ref}}}(v), \tag{3}$$

where ~~,~~ $P_{I_{\mathrm{ref}}}(v)$ is the normalized power output~~; $\overline{P(v)}$~~, $\overline{P}(v)$ is the measured ~~power output; $\overline{P_{\mathrm{sim},I}(v)}$~~ mean power, $\overline{P}_{\mathrm{sim},I}(v)$ is the simulated average power ~~output based on the real wind distribution using the zero TIpower curve, and $\overline{P_{\mathrm{sim},I_{\mathrm{ref}}}(v)}$~~ under the observed TI, and $\overline{P}_{\mathrm{sim},I_{\mathrm{ref}}}(v)$ is the simulated average power ~~output at the I_{ref} based on the Gaussian wind speed distribution using the zero TIpower curve~~under the reference TI.

3.5 Correlation and linear regression slope analysis

The correlation analysis serves a dual purpose. First, it ~~aims to elucidate~~ elucidates the relationship between power production and inflow conditions at different locations within the wind farm. Second, it evaluates the effectiveness of IEC corrections within the wind farm, which ~~falls~~ lies outside the current scope of the standard. To achieve these objectives, a Sliding Window Pearson Correlation (SWC) approach was employed. We compute the SWC as follows: (1) sort all 10 min records by nacelle wind speed v; (2) define a fixed window of width $0.75\,\mathrm{m\,s^{-1}}$; (3) within each window, compute the Pearson correlation between the variable of interest and the power deviation P_D; (4) assign this correlation to the mean v of that window; and (5) slide the window forward with one-third overlap and repeat.

The window is advanced by $\Delta u = 0.25\,\mathrm{m\,s^{-1}}$ (one third of the $0.75\,\mathrm{m\,s^{-1}}$ width) and evaluate only windows with at least $N_{\mathrm{min}} = 500$ records. In practice, retained windows typically contain $N \gtrsim 4\times10^3$ paired 10 min records, so even small correlations have a 95% significance threshold. This corresponds to a critical value of about $|r| \gtrsim 0.03$. Mild serial dependence would reduce the effective sample size slightly and raise this threshold, but not enough to affect the conclusions.

We analyze windows whose mean falls in $0.35 \le \hat{v} \le 1.20$, spanning region II (torque control) and region III (pitch control). Because the control state of a wind turbine ~~is highly dependent~~ depends strongly on wind speed during normal operation, the ~~data are first sorted by wind speed, and the~~ sliding window is applied along ~~this dimension. Pairwise correlations are calculated within a sliding window with a width of 0.75 m s^{-1}. The correlations obtained~~ v. Correlations from each window are then plotted against ~~the~~ that window's mean wind speed~~of that window, which allow the identification of~~, which reveals how the relationship between environmental variables and power production shifts across different wind speeds, both before and after the correction. ~~Similarly~~

Similar to the correlation analysis, we ~~computed~~ compute the linear regression slope of ~~TI~~ the normalized active power deviation with respect to ~~the~~ TI. The normalized active power deviation ~~, defined as $PD_{\text{norm}} = \frac{PD}{\text{rated power}}$~~ is defined as $PD_{\text{norm}} = PD/P_{\text{rated}}$, where PD is the active power deviation. This slope provides ~~another~~ an additional measure to assess the performance of the TI correction. By plotting the slope against the mean wind speed for each window, both before and after the correction, we ~~can~~ observe how the sensitivity of active power to TI changes with wind speed. This approach ~~thereby complements the insights gained from the~~ complements the correlation analysis by evaluating the effectiveness of the correction in reducing the influence of TI on power output.

3.6 Power curve variability analysis

While correlation analysis is useful for examining whether an environmental parameter influences power output before and after a correction, it has its limitations. Applying a correction can sometimes introduce noise that reduces the observed correlation between the environmental parameter and active power, effectively masking the true dependency. This means that relying solely on correlation analysis may not fully capture the impact of the correction. To more effectively assess the effect of a correction, we propose examining the variability of active power at different wind speeds across various sections of the wind farm, both before and after the correction. Specifically, we use the Median Absolute Deviation (MAD), as shown in Equation (4). This approach allows us to identify how the corrections affect the variance of the power curve. Moreover, MAD is less sensitive to outliers, making it a robust measure for this analysis.

$$\text{MAD}_{P_j} = \text{median}\left(|P_{j,i} - \text{median}(P_j)|\right) \tag{4}$$

where $P_{j,i}$ is the active power measurement i at wind speed bin j; and $\text{median}(P_j)$ is the median of all active power measurements at wind speed bin j.

4 Results and discussion

This section analyzes the influence of environmental parameters—wind shear, veer, and TI—on power production in different sections of the wind farm, both before and after applying IEC corrections. Three main types of plots are utilized: (1) Pearson correlation plots that show the relationship between each environmental parameter and active power across wind speed windows; (2) Corresponding Pearson correlation plots for the corrected values, which allow for an assessment of the effectiveness of the corrections; and (3) for TI, additional linear regression slope plots that evaluate the sensitivity of active power to TI before and after the correction. In the correlation plots the markers are shown only when the correlation is statistically significant (95% confidence).

In interpreting the correlation results, it is important to recognize that pairwise Pearson coefficients are expected to be modest in operational data, because multiple inflow parameters (wind speed, TI, shear/veer, stability), wake interactions, and active control jointly govern power. Our correlations target secondary inflow descriptors (TI, shear, veer) rather than the primary driver (wind speed), so small $|\rho|$ values are not only expected but consistent with offshore field evidence (peak values $\sim$0.16–0.21) (Seifert et al., 2021). Low $|\rho|$ does not imply irrelevance: when conditioned appropriately, shear and veer still produce statistically significant shifts in power (e.g., REWS-based segregation yielding departures of up to $\sim 5\%$ for a 1.5 MW turbine) (Murphy et al., 2020). We therefore emphasize the structure of the correlation profiles, sign changes across wind-speed bands, regime dependence (torque–to–pitch transition), front–mid–rear contrasts, and pre/post-correction trends, rather than the absolute magnitudes alone.

A related caveat is farm-scale blockage, which manifests primarily as a quasi-uniform reduction in upstream wind speed on several rotor diameters - measured at $\sim 3.4\%$ at $2D$ and $\sim 1.9\%$ at 7–$10D$ in onshore field campaigns (Bleeg et al., 2018), and observed offshore with lidar scanning such as $\lesssim 2\%$ extending tens of rotor diameters upstream (Schneemann et al., 2021). In this study, our analyses are conditioned on local inflow descriptors (TI, shear, veer) and on within-bin power variability, so a nearly uniform speed shift is not expected to alter the conditional relationships or the comparative conclusions about the IEC normalizations. Nevertheless, a dedicated, quantitative blockage assessment or applying published blockage corrections could refine absolute power levels and AEP estimates and is left for future work.

4.1 Wind shear and veer correction

Figures 4 and 5 illustrate the correlation of wind shear with active power before and after applying the REWS (shear-only) correction. A key observation is that the correlation patterns between wind shear and power production change depending on the position within the wind farm. Specifically, the influence of the ~~free-flow~~ free-stream incoming wind shear is most pronounced in the front section, with its influence weakening further downstream. Negative correlations are observed in the front row, while positive correlations appear in the rear section. This shift may be explained by changes of the ~~free-flow~~ free-stream wind profile as it moves through the farm, where wind turbine wakes enhance mixing and alter the shear and veer characteristics, however further investigation is required to understand the mechanism.

Figure 5 shows that even though the REWS correction is applied based on the time-averaged inflow profile, it ~~fails to reduce~~ reduces the correlation with the wind shear on the front section ~~or within the wind farm. This could be a result of the small correction that the REWS applies to the wind speed as suggested on (Van Sark et al., 2019)~~while it increases the apparent coupling in the mid and rear sections. In our case, based on the available measurements, the average correction is approx. $0.1\ \mathrm{m\ s^{-1}}$, with a standard deviation of $0.08\ \mathrm{m\ s^{-1}}$

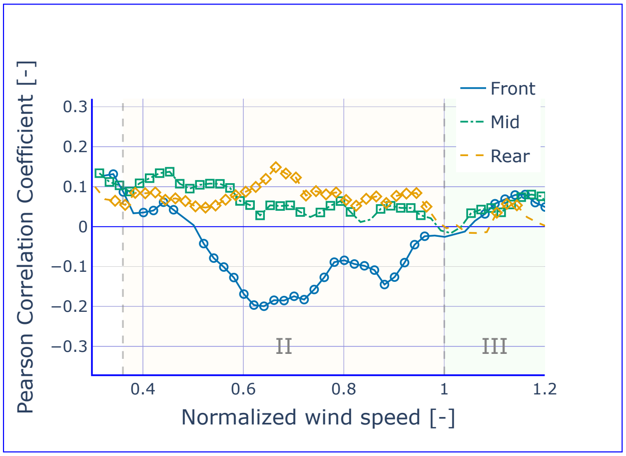

Figure 4. ~~(a) Correlation~~ Sliding-window correlation between wind shear α and ~~active~~ power ~~output at various wind speeds~~ deviation PD before ~~applying the~~ REWS~~normalization~~; markers shown only if $p < 0.05$.

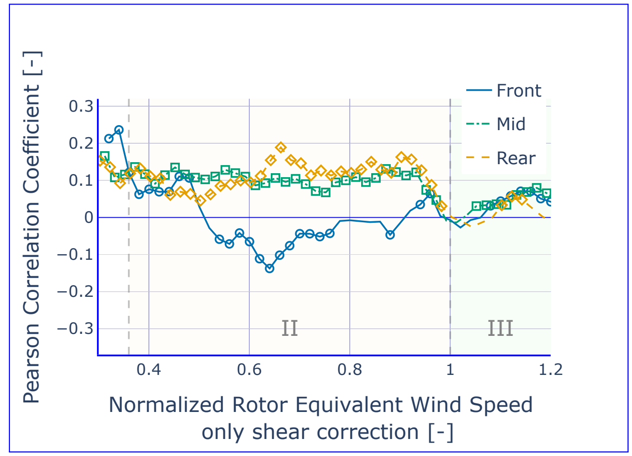

Figure 5. ~~Correlation~~ Sliding-window correlation between wind shear α and ~~active~~ power ~~output at various wind speeds~~ deviation PD after ~~applying~~ REWS (shear-only) correction; changes across the normalized REWS ~~normalization only for shear~~indicate where coupling is reduced or enhanced.

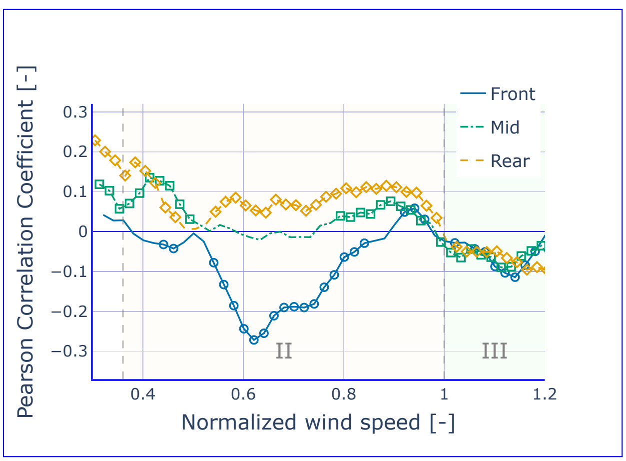

Figure 6. ~~Correlation~~ Sliding-window correlation between wind veer β and ~~active~~ power ~~output at various wind speeds~~ deviation PD before ~~applying the~~ REWS~~normalization~~ ; markers shown only ~~for veer~~if $p < 0.05$.

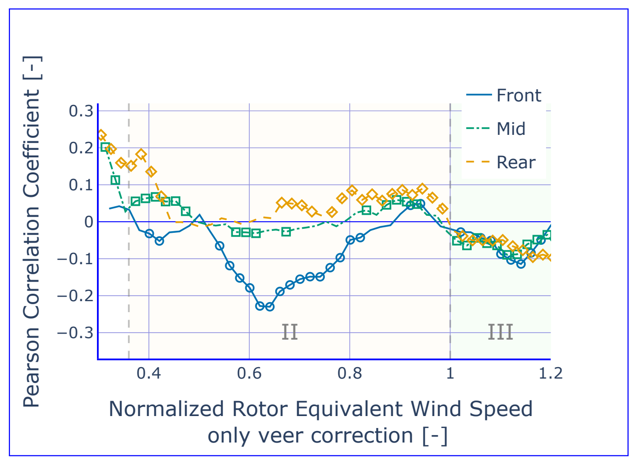

Figure 7. ~~Correlation~~ Sliding-window correlation between wind veer β and ~~the~~ power deviation ~~at various wind speeds~~ PD after ~~applying~~ REWS (veer-only) correction; changes across the normalized REWS ~~normalization only for veer~~indicate where coupling is reduced or enhanced.

Although the distance to measure wind shear and veer is relatively short for an offshore setting, obtaining more precise data closer to the wind farm - without assuming a wind shear profile based on power law Debnath et al. (2021) - may improve the correction. Another possible explanation is that shear and veer are correlated with other factors, such as turbulence intensity, which also affect power output. This interdependence makes it challenging to correct using REWS alone.

~~Similarly, the~~ The full veer–power correlation profiles before applying any correction and after applying the REWS (veer-only) correction are shown in Figures 6 and 7, respectively. The correlation patterns between wind veer and power output change depending on the position within the wind farm. In the front section, wind veer is negatively correlated with turbine power output, while positive correlations are observed in the rear section. Given that veer is linked with shear as described by Kelly and van der Laan (2023), our results suggest that both parameters exert a similar spatially dependent correlation with turbine performance. The REWS correction has a small impact on the effect of wind veer in the front section but does not decouple the correlation of inflow of ~~free stream~~ free-stream wind veer from the power output of the wind turbine. This could be a result of the small correction that the REWS applies to the wind speed as suggested by (Van Sark et al., 2019). It is important to note that the REWS correction is primarily designed to adjust for variations in the energy flux over the rotor due to wind shear and veer. However, the wind profile can also affect the aerodynamic load on the turbine blades. Consequently, even after applying the REWS correction, the residual correlation between wind veer or shear and power output indicates that these effects may not fully mitigated.

4.2 TI correction

Figures 8 and 9 compare the correlation between TI and wind turbine power output before and after applying the IEC-based correction at different locations within the wind farm. Additionally, figures 10 and 11 illustrate the sensitivity of the active power to TI by presenting the slope β of the linear regression between TI and normalized PD. These slopes are computed over the same $0.75\,\mathrm{m\,s^{-1}}$ windows with a $0.25\,\mathrm{m\,s^{-1}}$ stride, with typical window sizes exceeding 4×10^3 paired records. In figure 8, the correlation of TI at various wind speeds aligns with the expected behavior based on theoretical modeling (Saint-Drenan et al., 2020). Specifically, as expected by the literature, the front section has a positive correlation for normalized wind speeds 0.36–0.84 and a negative correlation at higher wind speeds. However, the rear sections have significantly different behavior for normalized wind speeds of up to 0.84. Although the negative correlations are initially small at wind speeds below 0.7, they become considerably stronger as the wind speeds approach the rated value. All sections have similar behavior at normalized wind speeds greater than 0.84; however, there are significant differences at lower wind speeds. Although all sections exhibit similar behavior at normalized wind speeds greater than 0.84, the significant differences at lower wind speeds suggest that the turbulent characteristics in the ~~free-flow~~ free-stream region are significantly different from those in the waked region.

The slope analysis presented in figure 10 complements the correlation findings by quantifying the sensitivity of PD to TI. The slopes β indicate how much the PD changes with a unit change in TI. The front section shows a small positive slope in the normalized wind speed range of 0.4 to 0.65, indicating a positive effect of TI on power. In contrast, in the same wind speed ranges, the mid and rear sections show lower slopes, indicating that these sections of the wind farm have a lower sensitivity to TI compared to the front section at low wind speeds. However, for normalized wind speeds above 0.84, all sections show a higher sensitivity to TI.

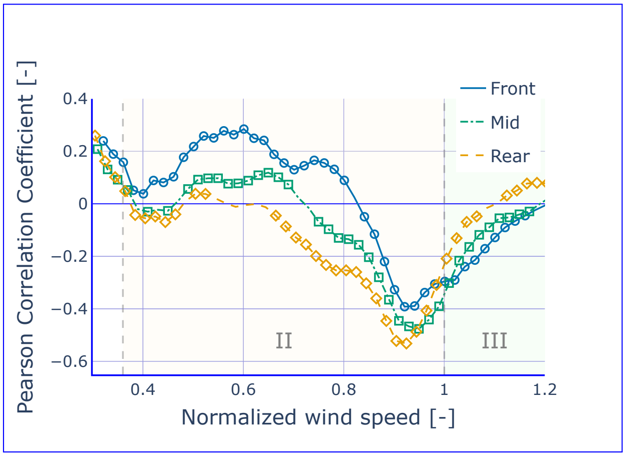

Figure 8. ~~Correlation~~ Sliding-window correlation between TI and ~~active~~ power ~~output at various wind speeds~~ deviation PD before ~~applying the~~ TI normalization; markers shown only if $p < 0.05$.

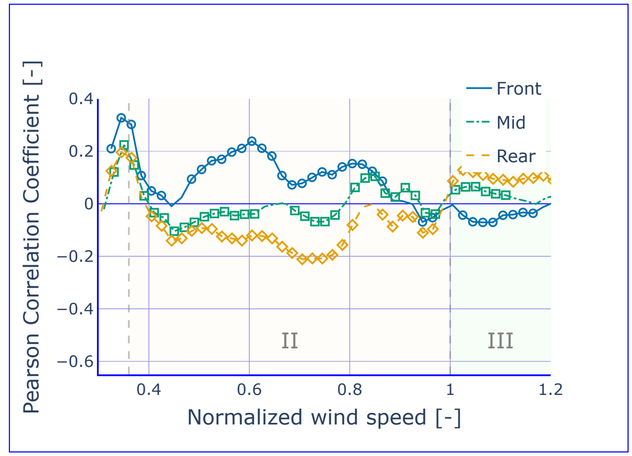

Figure 9. ~~Correlation~~ Sliding-window correlation between TI and ~~active~~ power ~~output at various wind speeds~~ deviation PD, after ~~applying the~~ TI normalization; changes across the normalized wind speed indicate where coupling is reduced or enhanced.

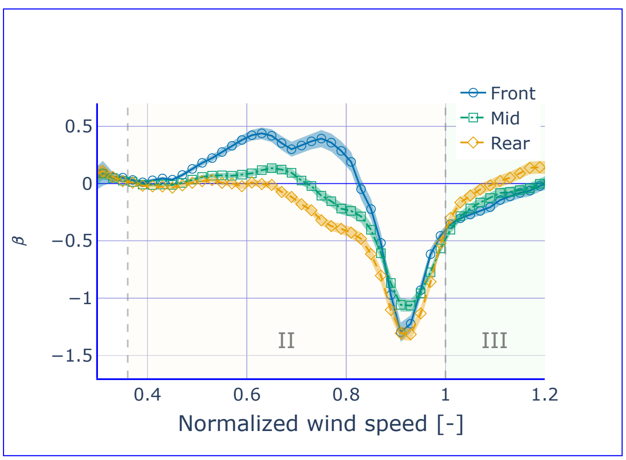

Figure 10. Linear regression slope between TI and active power output at various wind speeds before applying the TI normalization.

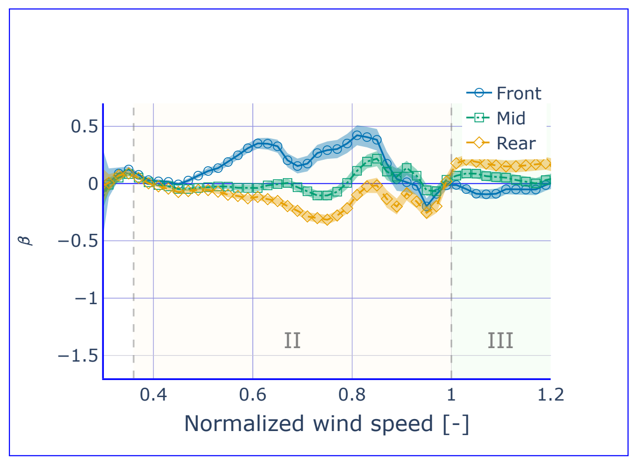

Figure 11. Linear regression slope between TI and active power output at various wind speeds after applying the TI normalization.

The results of the IEC correction in figure 9 indicate that, in the front and mid sections, the IEC correction reduces the correlation by about half for normalized wind speeds between 0.4 and 0.6, and further decreases TI dependency for wind speeds greater than 0.8. However, the correction behaves differently in the rear sections, where it overcompensates for TI effects and even shifts the correlation to the negative side for a wind speed lower than 0.6. For normalized wind speeds above 0.84, the correction appears to eliminate most of the TI dependency.

Similarly, the slope analysis in figure 11 shows that the sensitivity of PD to TI is significantly reduced after the correction in all sections for high wind speeds. For low wind speeds in the rear section, the slopes become more negative or remain low, indicating that the correction may be overcompensating or not adequately accounting for wake-induced turbulence effects. The overcompensation observed in the rear sections may be due to the increased wake-induced turbulence, which might differ significantly from the free-stream turbulence conditions assumed in the IEC correction methodology.

This suggests that the IEC TI correction may not be fully applicable within the wake-affected regions of the wind farm. However, it can still significantly correct for a large part of the TI effect on power production.

4.3 Effect on the variability of the power curve

To further examine how turbine location affects power production, we quantified the variability of active power in each section using the MAD. First, we established a baseline for each section (Figure 12) representing the variability before any corrections. In contrast, the rear section exhibits less variability than the front section, despite the presence of wakes and increased turbulence inside the wind farm.

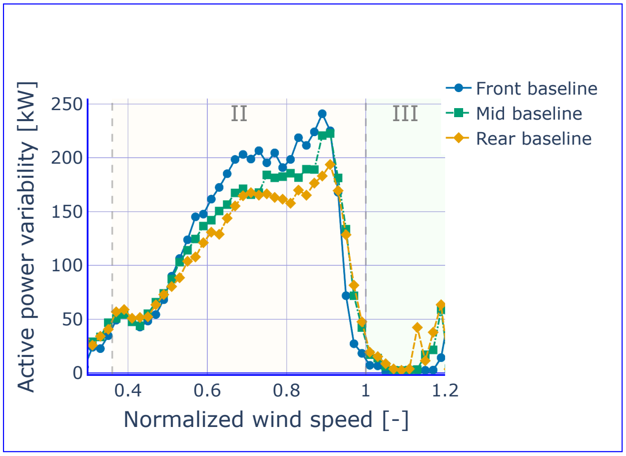

Figure 12. MAD of active power output across different wind speed bins for the different sections of the wind farm. The baseline curve represents the power curve MAD without any corrections.

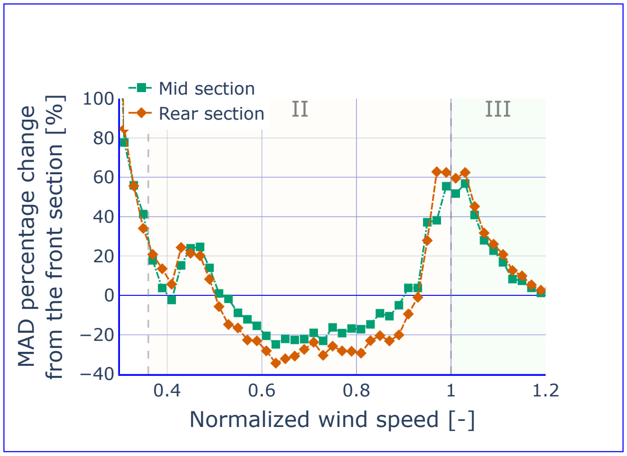

Figure 13. Percentage change in the MAD of active power output for the mid and rear sections compared to the front section.

For clarity, figure 13 shows the percentage change in MAD between the mid and rear sections compared to the front section. Both sections show reduced active power variability for normalized wind speeds between 0.64 and 0.92, with the rear section showing reductions of ~~up to 40%~~more than 30%. Next, we evaluated how the applied corrections influence this variability. Figure 14 illustrates the changes in MAD after each correction for each section. Overall, the corrections result in relatively

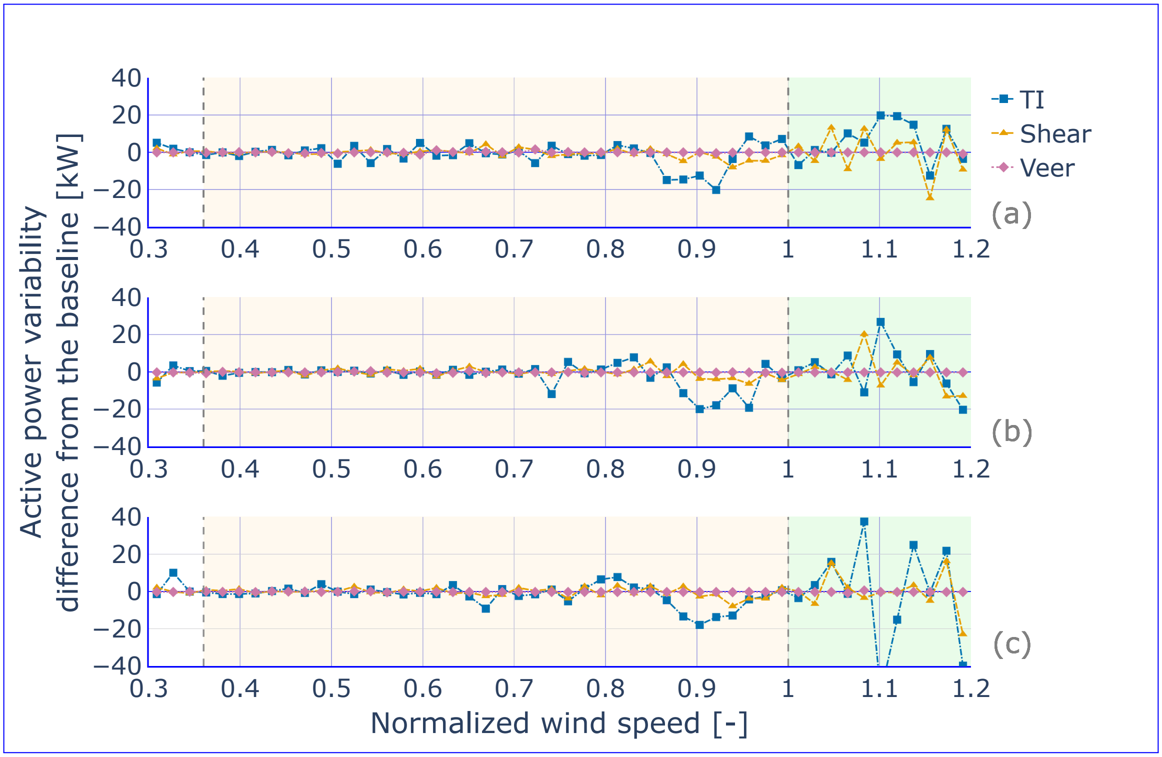

Figure 14. Differences in the MAD of active power output after each correction from the baseline across different wind speed bins. (a) Differences in the front section, (b) in the mid section, and (c) in the rear section of the wind farm.

small changes in MAD, with the only significant reduction in active power variability occurring from the TI correction for below-rated conditions.

4.4 Evaluation of correction-induced correlation changes

To visualize how each correction affects the correlation between environmental factors and power output, figures 15, 16, and 17 present the absolute change in correlation in the front, mid, and rear sections of the wind farm. The metric shown is ~~$(|\rho_{\text{after correction}}| - |\rho_{\text{before correction}}|)$~~ the absolute-correlation shift $\Delta|\rho| \equiv |\rho_{\text{corrected}}| - |\rho_{\text{uncorrected}}|$ where ρ is the Pearson correlation coefficient, as a function of wind speed, with different lines representing the corrections for wind shear, veer, and TI. Negative $\Delta|\rho|$ means the correction reduced the apparent coupling; positive means it increased.

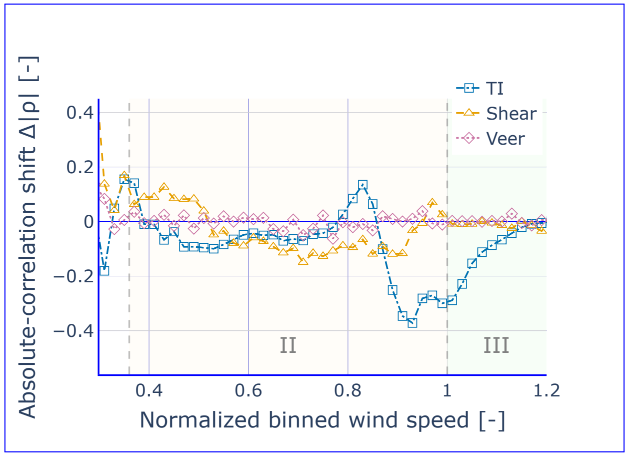

Figure 15. ~~Change~~ Front section: change in ~~the~~ correlation magnitude ~~of~~ relative to the ~~correlation between environmental factors and power output before and after applying corrections~~uncorrected baseline, ~~plotted against~~ $\Delta|\rho|$, versus wind speed~~for the front section of the wind farm~~.

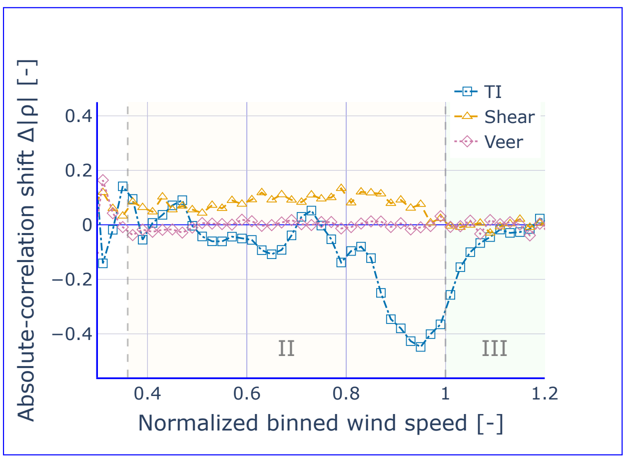

Figure 16. ~~Change~~ Mid section: change in ~~the~~ correlation magnitude ~~of~~ relative to the ~~correlation between environmental factors and power output before and after applying corrections~~uncorrected baseline, ~~plotted against~~ $\Delta|\rho|$, versus wind speed~~for the mid section of the wind farm~~.

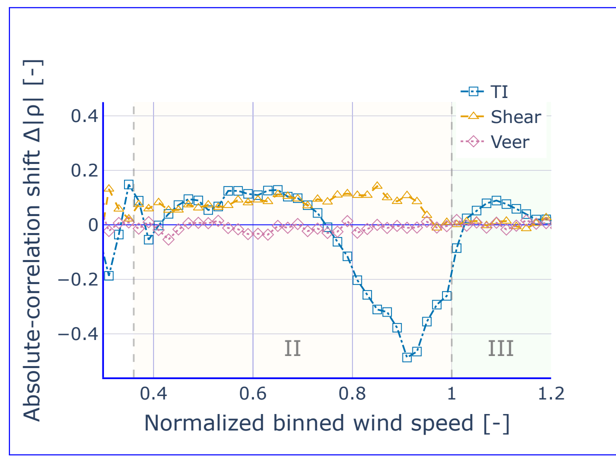

Figure 17. ~~Change~~ Rear section: change in ~~the~~ correlation magnitude ~~of~~ relative to the ~~correlation between environmental factors and power output before and after applying corrections~~uncorrected baseline, ~~plotted against~~ $\Delta|\rho|$, versus wind speed~~for the rear section of the wind farm~~.

As shown in these figures, the REWS corrections for wind shear and veer offer ~~minimal reductions in correlation within~~ a small reduction in the correlation for the front section ~~.~~ for wind speeds above $v/v_{\text{rated}} \approx 0.6$ (fig. 15). However, for lower wind speeds the corrections increase the coupling (fig. 15). In the mid and rear sections, these corrections ~~may even~~ slightly increase the correlation ~~at lower wind speeds.~~(figs. 16 and 17). In comparison, the effect of the TI correction is ~~much~~ stronger. The TI correction has a smaller effect in the front section ~~, but it~~ (fig. 15) but becomes more significant in the mid and rear sections, particularly as wind speeds approach the rated value, while the picture is ~~not as~~ less clear for lower wind speeds ~~.~~ (figs. 15, 16, and 17).

5 Conclusion

~~Using 10 − minute SCADA data, we evaluated the dependence of power production on turbulence intensity (TI), wind shear, and wind veer across different sections of~~ This study was set out to provide a detailed empirical assessment of how inflow conditions and turbine location impact power production and the effectiveness of IEC corrections in a large offshore wind farm. ~~Our findings demonstrate that these environmental factors influence turbine power output differently based on their location within the farm. Specifically, we highlight the limitations of IEC-based corrections, namely the TI correction and the rotor equivalent wind speed (REWS), by comparing their effectiveness between free-stream turbines (frontsection) and wake-affected (~~Using 13 months of 10 min SCADA and the upstream nacelle-lidar profiles, we asked how vertical shear, directional veer and TI couple to power across the front, mid and rear sections ~~). **Wind Shear and Veer**: Our analysis reveals a clear negative correlation between wind shear and veer with power production in the front-section turbines, aligning with expectations for~~ of a large offshore wind farm, and how IEC 61400-12-1:2022 normalizations perform in these regimes. We find that inflow–power coupling is strongly location dependent, IEC-style normalizations reduce apparent coupling mainly near free-stream conditions~~. In contrast, turbines in the mid and rear sections exhibit a positive correlation, suggesting that higher shear and veer may enhance power production within~~ , and TI inside the wind farm ~~. This behavior is likely due to the redistribution of energy by front-section turbines, which reduces~~ behaves differently from free-stream TI below rated wind speed.

The influence of wind shear and veer ~~downstream. However, the absence of simultaneous wind shear measurements within the farm and the considerable distance of the nacelle LiDAR from the turbines limit our ability to fully explain this mechanism. Additionally, despite the large rotor sizes, the IEC-based REWS correction does not effectively model the relationship between shear, veer , and active power , showing minimal impact on altering the correlation between wind speed and active power across all farm sections.~~ ~~**Turbulence Intensity (TI)**: Our correlation analysis indicates that TIpositively correlates with active power when data from the front and mid sections are analyzed at low wind speeds (<0.8 of the ratedvalue), which is consistent with findings reported in the existing literature. However, in the~~ revealed a distinct spatial dependency. In the front row (free-stream), shear and veer correlate negatively with power, while in mid and rear rows the correlation is positive. This sign flip is consistent with wake-induced mixing that flattens vertical gradients and changes the effective inflow seen by downstream rotors. The REWS normalization has limited practical effect: it slightly reduces coupling in the front section but does not decouple shear/veer from power inside the farm and can even increase coupling downstream.

A similarly complex, location-dependent behavior was observed for TI. It shows the expected positive correlation with power at sub-rated wind speeds in front/mid sections and becomes negative near rated; in the rear section, TI ~~exhibits a negative correlation with active power, highlighting~~ is already negatively correlated at lower normalized speeds, indicating that wake-induced TI ~~affects power production differently compared to~~ differs from free-stream TI. ~~Furthermore, the IEC-based TI~~

~~correction successfully models the impact of TI at lower wind speeds for the frontand mid sectionsbut fails to do so for~~ The IEC TI correction performs well for wind speeds above $v/v_{\mathrm{rated}} \gtrsim 0.8$ across all sections and reduces sub-rated TI coupling in the front/mid sections. However, in the rear section ~~. At higher wind speeds(> 0.8 of rated), the IEC-based TI correction is effective across all sections. In general, under the free flow conditions considered by the IEC, the TI correction performs as expected.~~ ~~**Overall Power Production Variability**~~: ~~Our study demonstrates that the variability~~ at low speeds, the correction tends to overcompensate, as seen in Figure 17.

The analysis of power production variability showed that the MAD (Median Absolute Deviation) within wind-speed bins is lower in ~~the~~ mid and rear ~~sections compared to the front section, reflecting spatial differences in the flow conditions within the wind farm that are not fully captured by the available measurements. This reduced variability suggests that inflow conditions evolve significantly as the wind passes the farm, leading to more stable power output in the downstream turbines~~rows than in the front row, implying more stable downstream power inside wake at a given wind speed. Corrections have small effects on MAD overall, only the TI correction yields a noticeable reduction below rated wind speed.

These ~~findings underscore that turbines operating under non-free-flow conditions within a wind farm experience inflow characteristics that differ substantially~~ results highlight that inside wind farms, the inflow differs significantly from free-stream ~~scenarios. Consequently, current IEC-based normalization methods are insufficient for accurately correcting the effect of TI, shear and veer in wake-affected environments. To improve performance evaluations, it is essential to incorporate a wider range of inflow characteristics, such as~~ assumptions. While current IEC normalizations (REWS, TI) are useful near free-stream conditions, they can be insufficient or regime dependent in waked rows. Adding inflow descriptors beyond standard IEC parameters, e.g., turbulent kinetic energy (TKE) (Kumer et al., 2016) ~~, beyond standard IEC parameters. This includes a more detailed characterization of wake-induced turbulence and shear effects, which can enhance the accuracy of power curve predictions and reduce uncertainties in the technical design of large offshore wind farms~~could improve power-performance evaluations and reduce uncertainty for large offshore projects.

~~Overall, our study underscores the limitations of current flow characterization methods to accurately assess power performance in large-scale offshore wind farms. Although the TI correction for free flow wind turbines at wind speeds around the rated performs as expected, the results for the mid- and rear sections are mixed. This highlights the need for improved normalization and correction techniques tailored to the complex inflow conditions encountered within such environments. By addressing these challenges, the wind industry can more effectively optimize turbine performance, reduce operational costs through improved power curve estimations, and achieve greater reliability in meeting global renewable energy targets~~Finally, while these findings are robust, it is important to note the study's context. Pairwise correlations are inherently modest in operational data and the lidar was located offsite, which we screened and treated conservatively; these constraints likely make our reported couplings conservative rather than inflated. Overall, location-dependent inflow effects and regime-dependent normalization performance argue for farm-aware evaluation methods that extend beyond free-stream IEC assumptions when assessing turbines inside wakes.

6 Code/Data Availability

The data supporting the findings of this study are not publicly available due to confidentiality restrictions under non-disclosure agreements with the data provider.

7 Author contributions

KV undertook the tasks of data curation and formal analysis, as well as writing, reviewing, and editing the initial draft and the final manuscript. RM was responsible for analyzing the LiDAR data. PJD, LP, JvB, and JH provided supervision, validated the results, and contributed to the review and editing of the manuscript. Finally, JH secured the necessary funding for this work.

8 Competing interests

The authors declare that they have no conflict of interest.

9 Acknowledgements

The authors acknowledge the financial support via the MaDurOS program from VLAIO (Flemish Agency for Innovation and Entrepreneurship) and SIM (Strategic Initiative Materials) through SBO project Rainbow. The authors would moreover like to acknowledge the Energy Transition Funds of the Belgian Federal Government for their funding of the POSEIDON project. Finally, the authors acknowledge the support of De Blauwe Cluster through the project Supersized 5.0. This work used large language model software for spelling and grammar checks.

Appendix A: Nacelle lidar reconstruction and uncertainty

Methodology

The horizontal wind vector is reconstructed from the lidar's line-of-sight (LOS) measurements using a two-beam de-projection method. At each measurement height, this technique uses two quasi-simultaneous beams at symmetric azimuth angles ($\pm a = \pm 15°$) to solve for the horizontal wind components (u_i, v_i). This reconstruction relies on the following assumptions: (i) negligible vertical wind velocity ($w \approx 0$), (ii) mean yaw alignment of the nacelle with the incoming flow, and (iii) horizontal homogeneity of the wind field across the narrow probed sector Letizia et al. (2023).

Continuous-wave (CW) lidars, like the one used in this study, measure a range-weighted average of the LOS velocity over a probe volume that increases with distance. This spatial averaging, combined with the geometric limitations of LOS measurements, can smooth turbulence and introduce biases if not properly accounted for. Our reconstruction and subsequent averaging can mitigate these effects. While absolute TI may be attenuated, the structure of the results we interpret (e.g., sign changes with wind speed, front/mid/rear contrasts, and $\Delta|\rho|$ trends) is not expected to be sensitive to a nearly uniform attenuation of fluctuations. We nevertheless acknowledge residual bias as a limitation.

Shear, Veer, and Uncertainty Estimation

From the reconstructed wind vectors at each height, the vertical wind shear exponent (α) is estimated by fitting the wind speeds to a power-law profile, while the wind veer (β) is estimated from the slope of a linear fit to the wind direction profile, $\theta(z)$. The final veer is reported in degrees per 100 meters ($^\circ/100\,\mathrm{m}$).

Uncertainties are propagated from the instrument's LOS noise ($\sigma_v = 0.10\,\mathrm{m\,s^{-1}}$, as specified by the manufacturer) to the reconstructed wind speed and direction at each height. These propagated variances are then used as weights in a Weighted Least Squares (WLS) fit for the shear and veer parameters. The covariance matrix from the WLS solution provides the standard uncertainty for α and β for each instantaneous scan. For our measurement geometry (measurement plane distance from the optical head $R = 420\,\mathrm{m}$), the expanded uncertainties per scan for the shear and veer estimations on average are:

$$U_\alpha \approx 0.06 \quad \text{and} \quad U_\beta \approx 0.86\,^\circ/100\,\mathrm{m} \quad (k=2).$$

Uncertainty of 30-Minute Averages

The final operational estimates are 30-minute means. While the lidar samples at 1 Hz, we assume the period for an effective independent measurement is 1 minute to account for autocorrelation in the high-frequency data. This results in an effective number of independent samples, $n_{\text{eff}} = 30$, within each 30-minute average. The standard uncertainty of the 30-minute mean is found by scaling the uncertainty of a single 1-minute estimate by $1/\sqrt{n_{\text{eff}}}$, which yields the final expanded uncertainties reported in the main text:

$$U_\alpha \approx 0.01 \qquad U_\beta \approx 0.15\,^\circ/100\,\mathrm{m} \quad (k=2).$$

Appendix B: NORA3-based representativeness assessment

Dataset and Rationale

To test whether the upstream nacelle-lidar measurements are representative of the inflow in the wind farm front section, we used the NORA3 dataset as an independent external reference. NORA3 is the regional atmospheric reanalysis of MET Norway that provides gridded hourly wind fields over the North Sea Haakenstad et al. (2021); Haakenstad and Øyvind Breivik (2022). Here, NORA3 is used to assess spatial homogeneity between the lidar location and the farm and to define conservative thresholds for extreme shear and veer. No NORA3 variables enter the correlation or correction analyses.

Homogeneity assessment and filtering

For each hour, we derive vertical shear (α) and veer (β) from NORA3 at two points: (i) the nearest lidar grid cell and (ii) a the closest cell of the front section of the farm. The separation of these points is $\approx 23.5\,\mathrm{km}$. Shear α is estimated by a power-law fit of $U(z)$ across the available levels; veer is the linear slope of the unwrapped direction with height, reported as $\beta_{100} = 100\,\beta$ in $^\circ/100\,\mathrm{m}$. This yields paired hourly series $\{\alpha_{\mathrm{L}}(t), \alpha_{\mathrm{F}}(t)\}$ and $\{\beta_{\mathrm{L}}(t), \beta_{\mathrm{F}}(t)\}$, where subscripts L and F denote the lidar-proximal grid cell and the farm's front-section grid cell, respectively.

We compare the two locations using quantile-quantile (Q-Q) plots and coincident hour time series. As shown in Figures B1a and B1b, the Q-Q plots for both shear and veer show strong agreement between the two locations through the core of the distributions, with some expected divergence in the extreme tails. The time series (Figures B2a and B2b) further confirm that the two sites track each other well.

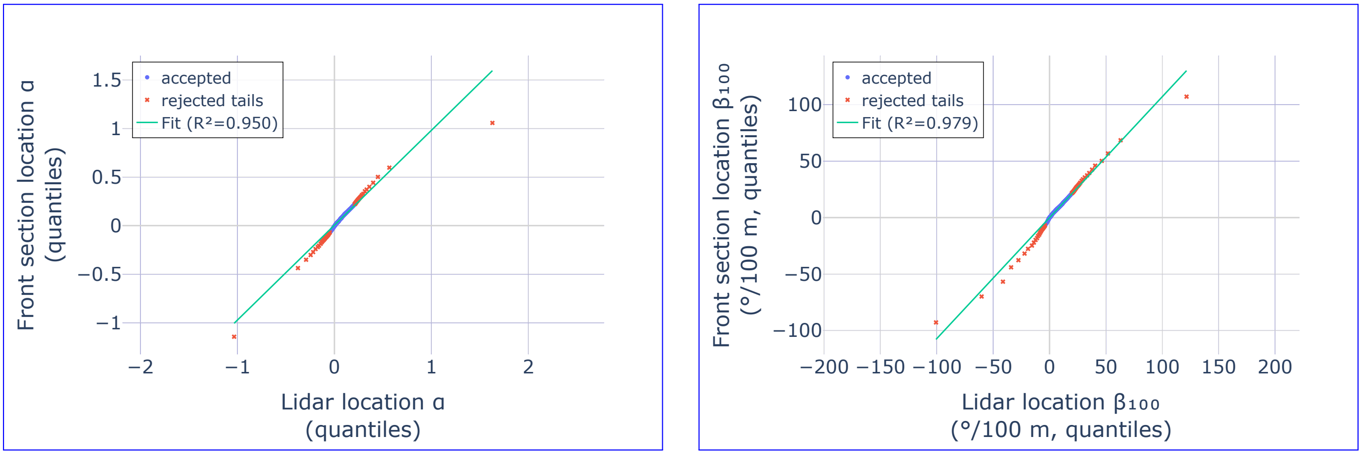

(a) Q–Q plot of hourly shear, α: lidar-nearest NORA3 grid cell (x-axis) vs. front-of-farm grid cell (y-axis). The solid line is an OLS fit with $R^2 = 0.95$.

(b) Q–Q plot of hourly veer, β_{100} (deg/100 m): lidar-nearest (x-axis) vs. front-of-farm (y-axis). The solid line is an OLS fit with $R^2 = 0.979$.

Figure B1. Q–Q comparisons between lidar-nearest and front-of-farm NORA3 grid cells.

This strong agreement validates the general representativeness of the lidar measurements. We therefore apply a conservative central 95% filter directly to the lidar-derived distributions of shear and veer, excluding the extreme tails where the NORA3 analysis indicates a higher potential for inhomogeneity. As specified in the main text, we keep the intervals as

$$\alpha \in [-0.05, 0.21], \qquad \beta_{100} \in [-3, 21]\ ^\circ/100\,\mathrm{m},$$

which are used as fixed limits in the study.

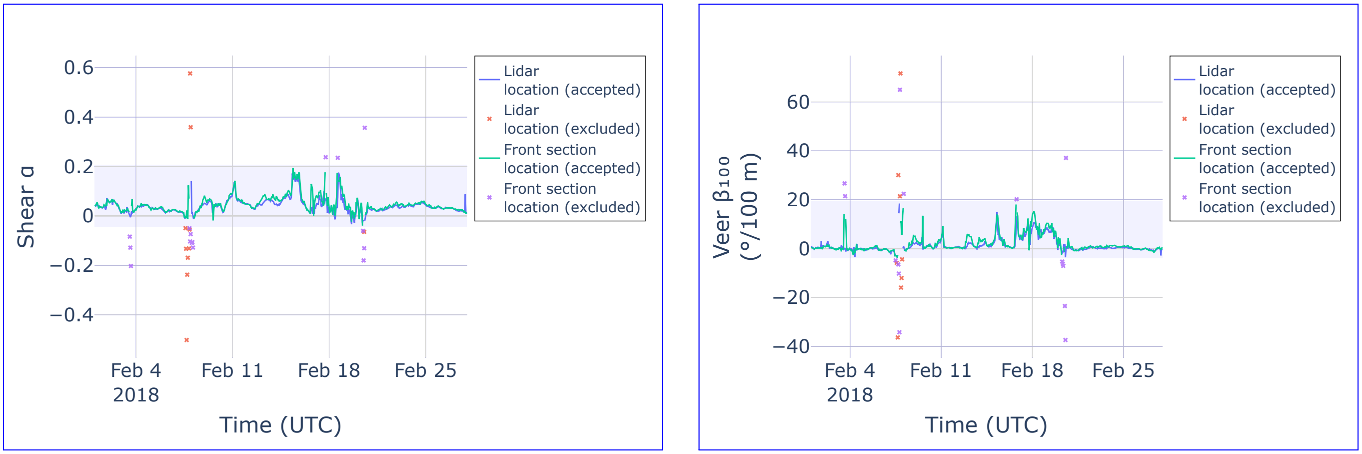

(a) Hourly time series of shear, α, at the lidar-nearest (blue) and front-of-farm (orange) NORA3 grid cells. The shaded band marks the retained central-95% limits ($\alpha \in [-0.05, 0.21]$) applied to the lidar data.

(b) Hourly time series of veer, β_{100} (deg/100 m), at the lidar-nearest (blue) and front-of-farm (orange) NORA3 grid cells. The shaded band marks the retained central-95% limits ($\beta_{100} \in [-3, 21]\,^{\circ}/100\,\mathrm{m}$) applied to the lidar data.

Figure B2. Hourly shear and veer at lidar-nearest and front-of-farm NORA3 grid cells.

References

IEC 61400-12-1:2022 Wind energy generation systems - Part 12-1: Power performance measurements of electricity producing wind turbines, Standard IEC 61400-12-1:2022, International Electrotechnical Commission, available at: webstore.iec.ch/publication/68499, 2022.

Adaramola, M. and Krogstad, P.-A.: Experimental investigation of wake effects on wind turbine performance, Renewable Energy, 36, 2078–2086, https://doi.org/https://doi.org/10.1016/j.renene.2011.01.024, 2011.

Bardal, L. M. and Sætran, L. R.: Influence of turbulence intensity on wind turbine power curves, Energy Procedia, 137, 553–558, https://doi.org/10.1016/j.egypro.2017.10.384, 14th Deep Sea Offshore Wind R&D Conference, EERA DeepWind'2017, 2017.

Barthelmie, R. J., Frandsen, S. T., Nielsen, M. N., Pryor, S. C., Rethore, P.-E., and Jørgensen, H. E.: Modelling and measurements of power losses and turbulence intensity in wind turbine wakes at Middelgrunden offshore wind farm, Wind Energy, 10, 517–528, https://doi.org/https://doi.org/10.1002/we.238, 2007.

Bleeg, J., Purcell, M., Ruisi, R., and Traiger, E.: Wind farm blockage and the consequences of neglecting its impact on energy production, Energies, 11, 1609, 2018.

Chamorro, L. P., Lee, S.-J., Olsen, D., Milliren, C., Marr, J., Arndt, R., and Sotiropoulos, F.: Turbulence effects on a full-scale 2.5 MW horizontal-axis wind turbine under neutrally stratified conditions, Wind Energy, 18, 339–349, https://doi.org/https://doi.org/10.1002/we.1700, 2015.

Cheynet, E., Diezel, J. M., Haakenstad, H., Breivik, Ø., Peña, A., and Reuder, J.: Tall wind profile validation of ERA5, NORA3, and NEWA datasets using lidar observations, Wind Energy Science, 10, 733–754, https://doi.org/10.5194/wes-10-733-2025, 2025.

Clifton, A. and Wagner, R.: Accounting for the effect of turbulence on wind turbine power curves, Journal of Physics: Conference Series, 524, 012 109, https://doi.org/10.1088/1742-6596/524/1/012109, 2014.

Commission, E.: REPowerEU Plan, https://ec.europa.eu/commission/presscorner/detail/en/ip_22_3131, accessed: 2024-09-06, 2022.

Congress, U.: Inflation Reduction Act of 2022, www.congress.gov/bill/117th-congress/house-bill/5376, accessed: 2024-09-06, 2022.

Debnath, M., Doubrawa, P., Optis, M., Hawbecker, P., and Bodini, N.: Extreme wind shear events in US offshore wind energy areas and the role of induced stratification, Wind Energy Science, 6, 1043–1059, 2021.

Dimitrov, N., Natarajan, A., and Kelly, M.: Model of wind shear conditional on turbulence and its impact on wind turbine loads, Wind Energy, 18, 1917–1931, https://doi.org/https://doi.org/10.1002/we.1797, 2015.

Gao, L., Li, B., and Hong, J.: Effect of wind veer on wind turbine power generation, Physics of Fluids, 33, 015 101, https://doi.org/10.1063/5.0033826, 2021.

González-Longatt, F., Wall, P., and Terzija, V.: Wake effect in wind farm performance: Steady-state and dynamic behavior, Renewable Energy, 39, 329–338, https://doi.org/https://doi.org/10.1016/j.renene.2011.08.053, 2012.

Gottschall, J. and Peinke, J.: How to improve the estimation of power curves for wind turbines, Environmental Research Letters, 3, 015 005, https://doi.org/10.1088/1748-9326/3/1/015005, 2008.

Haakenstad, H., Øyvind Breivik, Furevik, B. R., Reistad, M., Bohlinger, P., and Aarnes, O. J.: NORA3: A Nonhydrostatic High-Resolution Hindcast of the North Sea, the Norwegian Sea, and the Barents Sea, Journal of Applied Meteorology and Climatology, 60, 1443 – 1464, https://doi.org/10.1175/JAMC-D-21-0029.1, 2021.

Haakenstad, H. and Øyvind Breivik: NORA3. Part II: Precipitation and Temperature Statistics in Complex Terrain Modeled with a Nonhydrostatic Model, Journal of Applied Meteorology and Climatology, 61, 1549 – 1572, https://doi.org/10.1175/JAMC-D-22-0005.1, 2022.

Kelly, M. and van der Laan, M. P.: From shear to veer: theory, statistics, and practical application, Wind Energy Science, 8, 975–998, https://doi.org/10.5194/wes-8-975-2023, 2023.

Kim, D.-Y., Kim, Y.-H., and Kim, B.-S.: Changes in wind turbine power characteristics and annual energy production due to atmospheric stability, turbulence intensity, and wind shear, Energy, 214, 119 051, https://doi.org/10.1016/j.energy.2020.119051, 2021.

Kumer, V.-M., Reuder, J., Dorninger, M., Zauner, R., and Grubišić, V.: Turbulent kinetic energy estimates from profiling wind LiDAR measurements and their potential for wind energy applications, Renewable Energy, 99, 898–910, https://doi.org/https://doi.org/10.1016/j.renene.2016.07.014, 2016.

Lee, J. C. Y., Stuart, P., Clifton, A., Fields, M. J., Perr-Sauer, J., Williams, L., Cameron, L., Geer, T., and Housley, P.: The Power Curve Working Group's assessment of wind turbine power performance prediction methods, Wind Energy Science, 5, 199–223, https://doi.org/10.5194/wes-5-199-2020, 2020.

Letizia, S., Brugger, P., Bodini, N., Krishnamurthy, R., Scholbrock, A., Simley, E., Porté-Agel, F., Hamilton, N., Doubrawa, P., and Moriarty, P.: Characterization of wind turbine flow through nacelle-mounted lidars: a review, Frontiers in Mechanical Engineering, 9, 1261 017, 2023.

Martin, M., Pfaffel, S., te Heesen, H., and Rohrig, K.: Identification and prioritization of low performing wind turbines using a power curve health value approach, Journal of Physics: Conference Series, 1669, 012 030, https://doi.org/10.1088/1742-6596/1669/1/012030, 2020.

Mata, S. A., Pena Martínez, J. J., Bas Quesada, J., Palou Larrañaga, F., Yadav, N., Chawla, J. S., Sivaram, V., and Howland, M. F.: Modeling the effect of wind speed and direction shear on utility-scale wind turbine power production, Wind Energy, 27, 873–899, https://doi.org/10.1002/we.2917, 2024.

McCoy, A., Musial, W., Hammond, R., Mulas Hernando, D., Duffy, P., Beiter, P., Perez, P., Baranowski, R., Reber, G., and Spitsen, P.: Offshore Wind Market Report: 2024 Edition, Tech. rep., National Renewable Energy Laboratory (NREL), Golden, CO (United States), 2024.

McInnes, L., Healy, J., Astels, S., et al.: hdbscan: Hierarchical density based clustering., J. Open Source Softw., 2, 205, 2017.

Murphy, P., Lundquist, J. K., and Fleming, P.: How wind speed shear and directional veer affect the power production of a megawatt-scale operational wind turbine, Wind Energy Science, 5, 1169–1190, https://doi.org/10.5194/wes-5-1169-2020, 2020.

of Energy, U. D.: Land-Based Wind Market Report: 2024 Edition, https://www.energy.gov/sites/default/files/2024-01/Land-Based-Wind-Market-Report-2024.pdf, accessed: 2025-01-20, 2024.

Ren, Z., Verma, A. S., Li, Y., Teuwen, J. J., and Jiang, Z.: Offshore wind turbine operations and maintenance: A state-of-the-art review, Renewable and Sustainable Energy Reviews, 144, 110 886, https://doi.org/10.1016/j.rser.2021.110886, 2021.

Rohrig, K., Berkhout, V., Callies, D., Durstewitz, M., Faulstich, S., Hahn, B., Jung, M., Pauscher, L., Seibel, A., Shan, M., Siefert, M., Steffen, J., Collmann, M., Czichon, S., Dörenkämper, M., Gottschall, J., Lange, B., Ruhle, A., Sayer, F., Stoevesandt, B., and Wenske, J.: Powering the 21st century by wind energy—Options, facts, figures, Applied Physics Reviews, 6, 031 303, https://doi.org/10.1063/1.5089877, 2019.

Saint-Drenan, Y.-M., Besseau, R., Jansen, M., Staffell, I., Troccoli, A., Dubus, L., Schmidt, J., Gruber, K., Simões, S. G., and Heier, S.: A parametric model for wind turbine power curves incorporating environmental conditions, Renewable Energy, 157, 754–768, https://doi.org/10.1016/j.renene.2020.04.123, 2020.

Schneemann, J., Theuer, F., Rott, A., Dörenkämper, M., and Kühn, M.: Offshore wind farm global blockage measured with scanning lidar, Wind Energy Science, 6, 521–538, https://doi.org/10.5194/wes-6-521-2021, 2021.

Sebastiani, A., Peña, A., and Troldborg, N.: Numerical evaluation of multivariate power curves for wind turbines in wakes using nacelle lidars, Renewable Energy, 202, 419–431, https://doi.org/10.1016/j.renene.2022.11.081, 2023.

Sebastiani, A., Angelou, N., and Peña, A.: Wind turbine power curve modelling under wake conditions using measurements from a spinner-mounted lidar, Applied Energy, 364, 122 985, https://doi.org/10.1016/j.apenergy.2024.122985, 2024.

Seifert, J. K., Kraft, M., Kühn, M., and Lukassen, L. J.: Correlations of power output fluctuations in an offshore wind farm using high-resolution SCADA data, Wind Energy Science, 6, 997–1014, https://doi.org/10.5194/wes-6-997-2021, 2021.

Solbrekke, I. M., Sorteberg, A., and Haakenstad, H.: The 3 km Norwegian reanalysis (NORA3) – a validation of offshore wind resources in the North Sea and the Norwegian Sea, Wind Energy Science, 6, 1501–1519, https://doi.org/10.5194/wes-6-1501-2021, 2021.

Sumner, J. and Masson, C.: Influence of Atmospheric Stability on Wind Turbine Power Performance Curves, Journal of Solar Energy Engineering, 128, 531–538, https://doi.org/10.1115/1.2347714, 2006.

Van Sark, W. G., Van der Velde, H. C., Coelingh, J. P., and Bierbooms, W. A.: Do we really need rotor equivalent wind speed?, Wind Energy, 22, 745–763, https://doi.org/10.1002/we.2319, 2019.

Vratsinis, K., Pauscher, L., Daems, P.-J., Beeck, J. V., and Helsen, J.: Impact of inflow characteristics on the instantaneous power production using detrended fluctuation analysis, Journal of Physics: Conference Series, 2767, 092 071, https://doi.org/10.1088/1742-6596/2767/9/092071, 2024.

Wagner, R., Antoniou, I., Pedersen, S. M., Courtney, M. S., and Jørgensen, H. E.: The influence of the wind speed profile on wind turbine performance measurements, Wind Energy, 12, 348–362, https://doi.org/10.1002/we.297, 2009.

Wagner, R., Courtney, M., Gottschall, J., and Lindelöw-Marsden, P.: Accounting for the speed shear in wind turbine power performance measurement, Wind Energy, 14, 993–1004, https://doi.org/10.1002/we.509, 2011.

World Wind Energy Association: WWEA Annual Report 2024, https://wwindea.org/HYR2024, accessed: 2025-01-27, 2024.